Highly Photoluminescent Polyoxometaloeuropate-Surfactant Complexes by Ionic Self-Assembly

Tierui Zhang,[a] Christian Spitz,[b] Markus Antonietti,[a] and Charl F. J. Faul*[a, c]

Abstract: Facile organization of the inorganic sandwiched heteropolytungstomolybdate $K_{13}[Eu(SiW_9Mo_2O_{39})_2]$ (**E**) into highly ordered supramolecular nanostructured materials by complexation with a series of cationic surfactants is achieved by the ionic self-assembly (ISA) route. The structure and phase behavior of the complexes were examined by IR spectroscopy, differential scanning calorimetry, optical microscopy, and small- and wide-angle X-ray scattering. This class of materials shows a number of interesting physicochemical properties, namely liquid-crystalline phases (both thermotropic and lyotropic) and strong photoluminescence. The photophysical behavior (fluorescence spectra, fluorescence lifetimes, fluorescence quantum yield) of the complexes differs widely in solid powders, films, and solutions. The amphiphilic cationic surfactants not only play a structural role but also have a strong influence on the photophysical properties of **E**. The photophysical behavior of **E** can in this way be easily modified by its organizational motifs.

Keywords: ionic self-assembly · liquid crystals · photoluminescence · polyoxometalates · surfactants

Introduction

Transition-metal polyoxometalates (POMs) are typical inorganic metal-oxide clusters that exhibit a wealth of topologies and chemical and physical properties. These materials find use and application in catalysis, medicine, electrodes, and materials science.[1,2,3,4] A recent trend in POM chemistry has been the fabrication of functional nanostructures by using POMs as the inorganic building blocks, specifically using ionic self-assembly. Ichinose et al.[5] have obtained composite materials with layered arrays of isopolyanions $V_{10}O_{28}^{6-}$ by an ion-exchange technique. Stein et al.[6] and Janauer et al.[7] have synthesized layered materials consisting of $H_2W_{12}O_{40}$ and single-tailed trimethylammonium bromide surfactants. Taguchi et al.[8] obtained hexagonally mesostructured material with lacunar Keggin $PW_{11}O_{39}^{7-}$ ions and dodecyltrimethylammonium bromide. Mingotaud et al.[9,10] reported the fabrication of dimethyldioctadecylammonium (DODA)/POM superlattice Langmuir–Blodgett (LB) films through ion complexation, which show interesting magnetic properties. Polarz et al.[11] analyzed the complexation of "ferris-wheel"-shaped giant POMs with double-tailed cationic surfactants and described the organized hexagonal mesophases formed. Volkmer and Kurth et al.[12,13,14] recently described novel strategies to alter the surface properties of two POMs, with retention of their structural integrity and intrinsic properties by exchanging the POM counterions with DODA. This led to the formation of so-called "surfactant-encapsulated clusters" (SECs). Bu et al.[15,16] investigated the influence of packing on the structure of Langmuir and LB films of SECs, and the influence of the evaporation rates of organic solvents on the structure of solvent-cast films of SECs. The photocatalytic and photochromic properties of POM-containing multibilayer systems were described by Moriguchi et al.[17] and Zhao et al.,[18] respectively. Jin et al.[19] reported a counterintuitive synthesis route to room-temperature robust "core-shell" supramolecular assemblies based on didodecylammonium bromide cationic surfactant vesicles and ring-shaped POM nanoclusters.

POMs containing lanthanide elements, such as Eu^{3+}, Tb^{3+}, Sm^{3+}, and Dy^{3+}, have attracted much attention owing to their excellent luminescence properties.[20] This makes them

[a] Dr. T. Zhang, Prof. Dr. M. Antonietti, Dr. C. F. J. Faul
Max Planck Institute of Colloids and Interfaces
Research Campus Golm, 14424 Potsdam-Golm (Germany)
Fax: (+49) 331 567 9502
E-mail: charl.faul@mpikg-golm.mpg.de

[b] Dr. C. Spitz
Institut für Physik, Universität Potsdam
Am Neuen Palais 10, 14469 Potsdam (Germany)

[c] Dr. C. F. J. Faul
New address:
School of Chemistry, Inorganic and Materials Chemistry
University of Bristol, BS8 1TS Bristol (UK)

Supporting information for this article is available on the WWW under http://www.chemeurj.org/ or from the author.

 DOI: 10.1002/chem.200400796

attractive for applications in which lanthanide elements are used, for example replacements for radioactivity, phosphors in displays and screens, liquid lasers, and fluorescent dyes.[21,22,23,24] Mixed-addenda POMs are formed by substitution of one or more W^{VI} or Mo^{VI} ions in POMs by another metal ion. The functional properties of POMs can be widely changed by variation of the addenda atoms. Lis and But[25] have found that $K_{13}[Eu(SiW_{11-x}Mo_xO_{39})_2]$ sandwiched compounds show strong luminescence owing to energy transfer from the hetero-polytungstomolybdate groups to the Eu^{3+} ion. The Eu^{3+} luminescence intensity of the complexes indicates an increase of the efficiency of the energy transfer from the hetero-polytungstomolybdate group to the Eu^{3+} ion as X decreases. However, if $X=0$, that is, $K_{13}[Eu(SiW_{11}O_{39})_2]$, energy transfer from the ligand to Eu^{3+} is not observed, and the luminescence intensity decreased by approximately 160 times compared with that of $K_{13}[Eu(SiW_9Mo_2O_{39})_2]$ at the same concentration.

In the previous preparation of organic/POM mesostructured materials, DODA was mostly used as the structure-directing agent, with few other surfactants used. The extension of those experiments to now include hybrid complexes built up with functional surfactants in combination with the POM tecton (or building block) carries the promise of new synergistically produced properties. Furthermore, it is also of importance to investigate the effects of different surfactants on the properties of the resulting POM hybrid materials. This should provide insight into the structure–property–function relationships that exist in such nanostructured materials.

Herein, we employ the ionic self-assembly (ISA)[26,27] route to generate nanostructured organic–inorganic hybrid materials from mixed-addenda $[Eu(SiW_9Mo_2O_{39})_2]^{13-}$ POMs and a variety of normal and functional organic surfactants. ISA has already been successfully employed to produce novel hybrid organic–inorganic nanostructured materials that exhibit interesting switching properties.[28,29] In general, the product of the ISA procedure is an organized nano(hybrid) structure that combines the properties of both components. Here this leads to the combination of the extraordinary optical and electronic properties of the POM species with the ability of the organic counterions to provide dissolution in organic solvents, transparent film formation, and the convenient orientation of LC species. In other words, ISA complexes allow the POM tectons to be brought into forms that are useful for materials application and that allow new chemical investigations. We focus on the photophysical properties of these functional hybrid systems in the solid, solution, and film states.

Results and Discussion

Characterization of the structure: We used FTIR to study the order of the alkyl chains in the complexes. Frequencies for the CH_2 antisymmetric $\nu_{as}(CH_2)$ and the symmetric stretching $\nu_s(CH_2)$ bands are sensitive to the conformation of the alkyl chains.[30,31] When the alkyl chains are highly ordered (all-*trans* conformation), the bands appear near 2918 and 2850 cm^{-1}, respectively. However, when the alkyl chains are highly disordered, the frequencies may shift upward to near 2927 and 2856 cm^{-1}. Hence, $\nu_{as}(CH_2)$ and $\nu_s(CH_2)$ can be used as practical indicators of the degree of order for alkyl chains. In the FTIR spectra of the complex, the $\nu_{as}(CH_2)$ and $\nu_s(CH_2)$ bands appeared around 2920 and 2850 cm^{-1}, respectively. Thus, the arrangement of hydrocarbon chains is well ordered (but not necessarily crystalline, see the X-ray analyses below), implying few *gauche* defects in the complexes. The bands around 3300–3500 and 1600–1650 cm^{-1} are assigned to stretching and bending modes of water, respectively. Strong bands are observed below 1010 cm^{-1} for vibrations originating from **E** ($K_{13}[Eu(SiW_9Mo_2O_{39})_2]$).[32] The bands associated with the anions in the complexes are generally slightly shifted when compared to those of the pure solid **E** in a KBr pellet. This demonstrates that polyanions are "trapped" in the complexes and that their chemical structure is not destroyed. The shifts of different peaks are related to the organization and especially to the presence of positively charged surfactants in the complexes.[33] Only minor differences were found in the IR spectra of complex solid powders and their respective films. The detailed assignments are summarized in Table 1.

Table 1. Frequency values (cm^{-1}) and assignments of infrared spectra of the complexes.

E/C_{16}D	**E**/C_{12}D	**E**/C_{16}T	**E**/C_{12}T	**E**/C_{15}F	**E**/C_{11}F	**E**/C_{18}D	**E**	Assignments[a]
3442	3449	3445	3443	3440	3441	3452	3423	ν_{as}(O–H)
2919	2922	2920	2921	2922	2923	2922		$\nu_{as}(CH_2)$
2850	2851	2850	2851	2851	2852	2851		$\nu_s(CH_2)$
1633	1631	1635	1632	1636	1636	1636	1616	δ(O–H)
996	991	999	997	1000	999	997	1005	$\nu_s(Si–O_a)$
940	940	941	943	940	939	938	943	$\nu_{as}(M–O_d)$
890	894	891	894	894	894	892	889	$\nu_{as}(M–O_b–M)$
812	804	810	806	804	805	816	823	$\nu_{as}(M–O_c–M)$
771	773	771	768	768	770	770	762	
722	722	720	728	721	722	722	717	

[a] as, asymmetric; s, symmetric; ν, stretching; δ, bending; M = W or Mo.

One strong characteristic absorption band of **E** at approximately 254 nm[34] is found in the UV/Vis spectra of films of these complexes. This corresponds to the charge-transfer (CT) transition of $O_{b(c)} \rightarrow M$ ($O_{b(c)}$ = bridge oxygen, M = W or Mo), substantiating the incorporation of the polyanions into the composite films without structural decomposition. Since the f→f bands of Eu^{3+} in the visible region are very weak and can only be seen in concentrated solutions,[35] the UV/Vis spectra of the composite films do not show these bands.

The thermal properties of these materials were investigated by thermogravimetric analysis (TGA) and differential

scanning calorimetry (DSC). TGA analyses revealed that the degradation temperature was generally above 220 °C for **E**/C_{16}D and **E**/C_{12}D complexes; 180 °C for **E**/C_{16}T, **E**/C_{12}T, and **E**/C_{18}D complexes, and 130 °C for **E**/C_{15}F and **E**/C_{11}F complexes. DSC analyses showed that, except for the **E**/C_{15}F and **E**/C_{11}F complexes, all complexes exhibit reversible thermal transitions. Figure 1 shows, as an example, the DSC

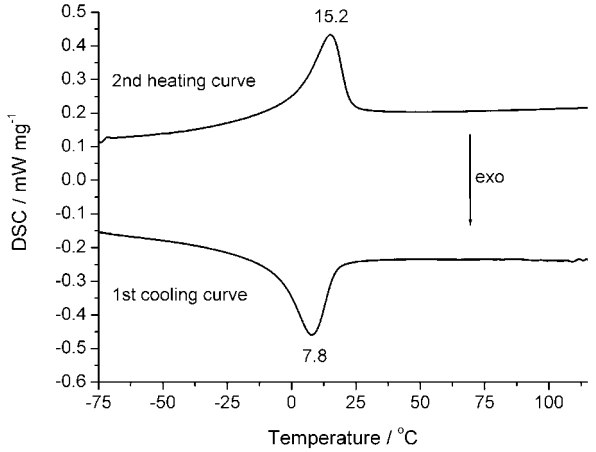

Figure 1. DSC curve of the **E**/C_{16}D complex.

curve of the **E**/C_{16}D complex. A strong endothermic transition ($\Delta H = 10.6$ kJ mol^{-1}) is found around 15.2 °C, which corresponds to a typical transition enthalpy of melting of alkyl chains.[36] As the length of the alkyl tail decreases, the transition temperatures and transition enthalpies decrease systematically. This provides further support for attributing this transition to structural rearrangements of the alkyl chains.

Further evidence for the conformational order of the surfactants in the complexes results from X-ray diffraction investigations. WAXS analyses showed no sharp reflections in the wide-angle region in all cases, and only two broad reflections at approximately 29.2° and 20.5° (18.8° for **E**/C_{15}F and **E**/C_{11}F complexes). The spacings are calculated to be 0.31 nm and 0.43 nm (0.47 nm). The broad reflection centered at 0.43 nm corresponds to the lateral packing of the alkyl chains, indicative of close (but not crystalline) packing of alkyl chains.[37] For the **E**/C_{15}F and **E**/C_{11}F complexes, the reflection at 0.47 nm indicates loosely packed alkyl chains, which results from the increased size of the ferrocene head group. These results correspond to the results from DSC investigations. The detailed assignments are summarized in Table 2.

Room-temperature SAXS analyses of the complexes (Figure 2) show the presence of a number of phases, including lamellar, hexagonal, and possibly a cubic phase (as assigned from the peak positions). The phase assignments and *d* spacings of the complexes are listed in Table 2. The absence of crystallization in the alkyl tails, combined with the mesoscopic order (as seen from SAXS) show that, even if solid materials, all the POM-surfactant complexes are by definition in a thermotropic liquid-crystalline state at room

Table 2. WAXS and SAXS experimental result of the complexes.

Sample	WAXS 2θ	WAXS spacing [nm]	SAXS spacing [nm]	Assigned phase
E/C_{16}D	20.82°, 29.18°	0.43, 0.31	4.31	Lam
E/C_{12}D	20.56°, 29.12°	0.43, 0.31	3.16	Lam
E/C_{16}T	21.08°, 29.31°	0.42, 0.31	3.65	(Cubic)[a]
E/C_{12}T	20.94°, 29.15°	0.42, 0.31	2.93	Hex
E/C_{18}D	20.29°, 28.85°	0.44, 0.31	3.45	Lam
E/C_{15}F	18.89°, 29.48°	0.47, 0.30	2.69	(unclear)[b]
E/C_{11}F	18.77°, 29.33°	0.47, 0.31	2.32	(unclear)[b]

[a] Due to the presence of weak diffractions at the $3^{1/2}$ and $5^{1/2}$ position, a clear assignment of the phase is not possible. [b] These phases could possibly be hexagonal phases, but a definite phase assignment cannot be made.

temperature. Temperature-dependent light microscopy investigations of all the materials showed no characteristic textures or transitions to the isotropic state. Melting of the materials only took place after the onset of degradation (visible color changes), at the temperatures as found in the TGA investigations.

However, the results show that we can control the phase and *d* spacing of the complexes by choosing different surfactants with different physical characteristics, such as differences in the length and the number of alkyl tails as well as the size and style of the head groups. In addition, there is not much difference between the SAXS patterns of the complex solids and films, respectively, which shows that they are isomorphous.

Lyotropic phase behavior: Only a few examples of lyotropic liquid-crystalline behavior are known in inorganic chemistry.[38,39,40] The reason for this might either be due to the absence of sufficient amphiphilicity in inorganic compounds or the lack of mobility to enable the adoption of a supramolecular conformation of minimal free energy.[11] As a consequence, it is an important challenge in chemistry to align inorganic objects into ensembles that display long-range order. Figure 3a is the optical photomicrograph (taken with crossed polarizers) of the lyotropic liquid-crystalline phase as observed from a contact preparation with chloroform. It shows pseudo-focal conic fan-shaped textures, which are characteristic for columnar phases.[41,42] The pseudo-focal conical fan-shaped texture gradually changes into a fibroid-like texture (Figure 3b), which is assigned to a change in the orientation of the columns parallel to the glass surface rather than to a new phase. The **E**/C_{12}D complex shows the same lyotropic liquid-crystalline phase behavior as that of the **E**/C_{16}D complex. The solutions of other complexes also exhibit birefringence under polarized optical microscopy. However, no typical textures could be identified and no additional information could be obtained.

Photoluminescent properties: Figure 4A shows the excitation spectra monitored for the $^5D_0 \rightarrow {}^7F_2$ transition for **E** (solid), **E**/C_{16}D (solid), and **E**/C_{16}D (film) on quartz. The excitation spectrum of **E** (solid) has the characteristic peaks of Eu^{3+} assigned to the $^7F_0 \rightarrow {}^5L_6$ (395 nm), $^7F_0 \rightarrow {}^5D_2$ (465 nm),

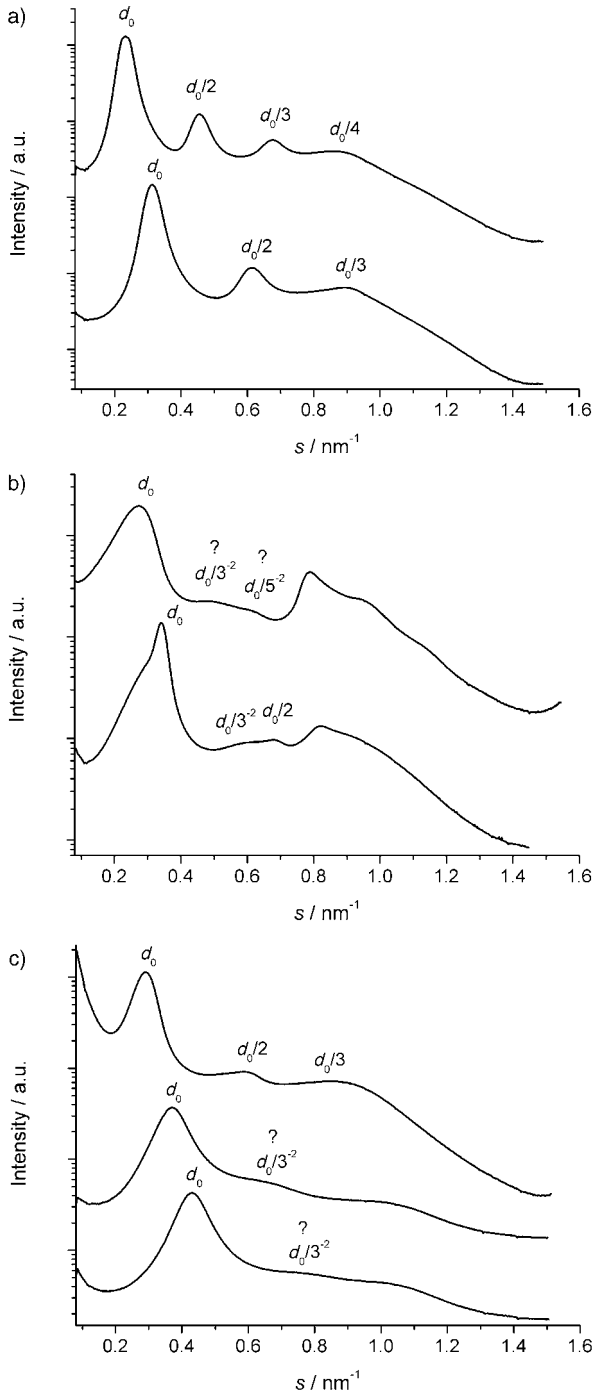

Figure 2. SAXS data of a) the **E**/C_{16}D (top) and **E**/C_{12}D (bottom) complexes; b) the **E**/C_{16}T (top) and **E**/C_{12}T (bottom) complexes; c) the **E**/C_{18}D (top), **E**/C_{15}F (middle), and **E**/C_{11}F (bottom) complexes.

and $^7F_0 \rightarrow {}^5D_1$ (526 nm, 535 nm) transitions and a wide symmetric band ranging from 235 to 435 nm ($\lambda_{max} = 355$ nm) corresponding to the O→M ligand-to-metal charge-transfer (LMCT) transition within the polytungstomolybdate ligand. This charge-transfer band plays an important role in the luminescence of **E** since photoexcitation of this transition leads to intramolecular energy transfer from $[SiW_9Mo_2O_{39}]^{8-}$

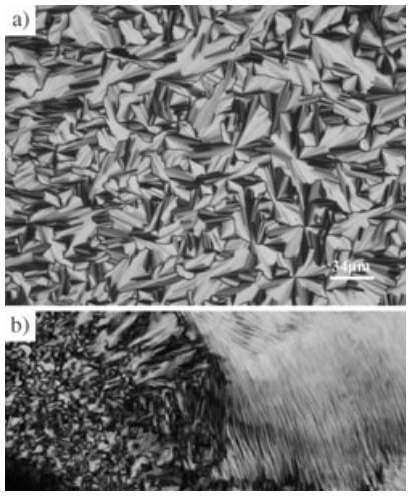

Figure 3. Optical textures of a) the hexagonal columnar mesophase of the **E**/C_{16}D complex in chloroform and b) the two typical textures observed. The fibroid-like texture is probably due to columns aligning parallel to the surface as observed under crossed polarizers.

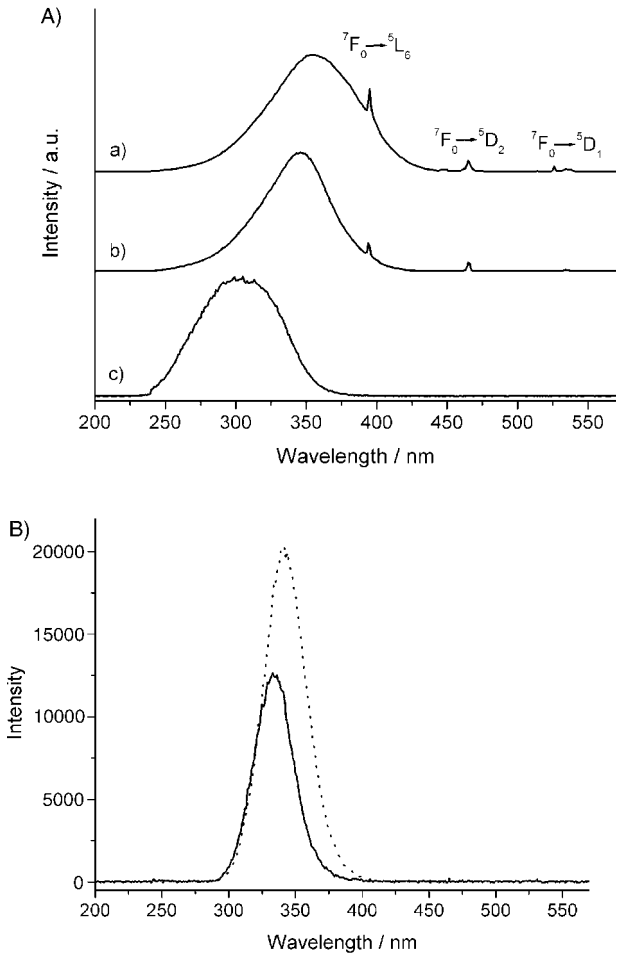

Figure 4. A) Excitation spectra of a) **E** solid, b) **E**/C_{16}D solid, and c) **E**/C_{16}D film on quartz monitored into the $^5D_0 \rightarrow {}^7F_2$ transition (614 nm). B) The excitation spectra of **E** (full line) and **E**/C_{16}D (dotted line) solution, concentration = 0.2 mmol L^{-1}, $T = 25$ °C.

to Eu^{3+}, followed by characteristic luminescence of Eu^{3+}.[43] In **E**/C_{16}D (solid), the characteristic transitions of Eu^{3+} become weaker and the LMCT band appears in the 235–420 nm region with a narrow maximum slightly blue-shifted to 346 nm. The intramolecular energy transfer from the excited state of the ligands to the emitting $^5D_0$ level of Eu^{3+} is strongly affected by the configuration of the surrounding ligands.[43,44] In **E**/C_{16}D (solid), the strong electrostatic interaction between the C_{16}D surfactants and **E** has an influence on the coordination environment of Eu^{3+}, and consequently changes the energy levels of the LMCT of the ligands. The characteristic transitions of Eu^{3+} can barely be detected from the spectrum of the solid, and the LMCT bands shift to higher energies with a maximum at 304 nm. It shows that the probability of radiative recombination between an electron and hole in the relaxation of the LMCT state decreases in the film, contributing to an increase in the probability of energy transfer to the Eu^{3+},[45] and therefore a further blue shift in the maximum. Our results seem to indicate that the particular orientation of the central **E** tecton induced by the film processing procedure is the main factor responsible for this effect. This is supported by the fact that no major structural difference between the solid and film could be detected by either detailed IR or X-ray analyses. As for the spectra of **E** and **E**/C_{16}D (solution) shown in Figure 4B, differences were observed from the corresponding solid (position, width, and shape) that may result from the influence of solvent molecules as well as the molecular orientation within the structured complex material. The assignment of the transitions found in the excitation spectra is summarized in Table 3.

Table 3. LMCT band (nm), the intensity ratio of the $^5D_0\rightarrow{}^7F_2$ transition to the $^5D_0\rightarrow{}^7F_1$ transition, experimental $^5D_0$ lifetime (τ, ms) and decay rate (k_{tot}, ms^{-1}), calculated radiative (k_r) and nonradiative (k_{nr}) $^5D_0$ decay rate (ms^{-1}) and quantum yield (η, %) for **E** and all the complexes in the different states (chloroform was used as solvent, except where indicated) at room temperature.

Sample	State	LMCT [nm]	$I(^5D_0\rightarrow{}^7F_2)/I(^5D_0\rightarrow{}^7F_1)$	τ	k_{tot}	k_r	k_{nr}	η
E	solid	355	2.04	2.083	0.480	0.252	0.228	52.5
	solution (water)	334	2.32	3.137	0.319	0.194	0.125	60.8
E/C_{16}D	solid	346	4.12	1.880	0.532	0.365	0.167	68.6
	film	304	3.65	1.526	0.655	0.353	0.302	53.9
	solution	342	11.27	1.163	0.860	0.706	0.154	82.1
E/C_{12}D	solid	354	5.13	1.974	0.507	0.424	0.083	83.7
	film	304	4.74	1.648	0.607	0.401	0.206	66.1
	solution	342	13.62	1.184	0.845	0.812	0.033	96.1
E/C_{16}T	solid	343	4.01	1.764	0.567	0.357	0.210	63.0
	film	314	4.09	1.480	0.676	0.382	0.294	56.5
	solution	340	4.47	1.634	0.612	0.346	0.266	56.5
	solution (MF)[a]	338	7.27	1.152	0.868	0.498	0.370	57.4
E/C_{12}T	solid	341	5.25	1.275	0.784	0.429	0.355	54.7
	film	328	5.95	1.119	0.894	0.509	0.385	57.0
	solution (MF)	339	7.05	1.189	0.841	0.500	0.341	59.5
E/C_{18}D	solid	338	3.20	0.591	1.692	0.339	1.353	20.0
	film	311	3.83	0.270	3.704	0.420	3.284	11.3
	solution (MF)	339	4.88	0.292	3.425	0.498	2.927	14.5
E/C_{15}F	solid	354	7.09	0.020	50.000	0.590	49.410	1.2
	film	313	6.31	0.017	58.824	0.478	58.346	0.8
	solution	345	12.59	–	–	0.753	–	–
E/C_{11}F	solid	352	7.33	0.033	30.303	0.598	29.705	2.0
	film	313	5.36	0.030	33.333	0.446	32.887	1.3
	solution	345	10.87	–	–	0.645	–	–

[a] MF = *N*-methylformamide.

The room-temperature emission spectra for **E** (solid), **E**/C_{16}D (solid), and **E**/C_{16}D (film) on quartz under excitation into the LMCT states are presented in Figure 5A. Each of the emission spectra exhibit the characteristic transitions of Eu^{3+}, which are due to transitions within the $4f^6$ electron shell and attributed to energy-level transitions from the $^5D_0$ metastable state to various terminal levels, mainly $^5D_0\rightarrow{}^7F_j$ ($j=0$, 1, 2, 3, 4) transitions. Obvious changes of some emission peaks can be observed for the **E**/C_{16}D (solid) and **E**/C_{16}D (film) compared with **E** (solid). The symmetry-forbidden emission $^5D_0\rightarrow{}^7F_0$ at 581 nm can be discerned with low relative intensity in **E** solid. The emission is enhanced in **E**/C_{16}D (solid) and **E**/C_{16}D (film), with a slight blue shift to 580 nm. The presence of only one peak suggests the existence of one local site symmetry for the chemical environment of the Eu^{3+} ion. The energy of the $^5D_0\rightarrow{}^7F_0$ transition is usually correlated with nephelauxetic effects arising from the Eu^{3+} first neighbors, so that variations detected in its energy indicate variations in the Eu^{3+} first coordination sphere, namely, the number and/or type of the Eu^{3+} ligands.[46,47] It may indicate that structural changes are induced in the Eu^{3+} local coordination site with surfactant complexation. Another remarkable change is that the intensity ratio of the $^5D_0\rightarrow{}^7F_2$ transition to the $^5D_0\rightarrow{}^7F_1$ transition in **E** (solid) is quite different from that in **E**/C_{16}D (solid) and **E**/C_{16}D (film). The $^5D_0\rightarrow{}^7F_1$ transition is a magnetic dipole transition and its intensity hardly varies with the crystal field strength acting on Eu^{3+}. On the other hand, the $^5D_0\rightarrow{}^7F_2$ transition is an electric dipole transition and is extremely sensitive to chemical bonds in the vicinity of the Eu^{3+} ion. The intensity of the $^5D_0\rightarrow{}^7F_2$ transition increases as the site symmetry of Eu^{3+} decreases.[48,49] Therefore, the intensity ratio of the $^5D_0\rightarrow{}^7F_2$ transition to the $^5D_0\rightarrow{}^7F_1$ transition is commonly used to study the chemical microenviroment of anions coordinating the Eu^{3+} ions and is used as a measure of the rare-earth site symmetry. However, it should be kept in mind that this ratio is also influenced by other factors such as the polarizability of the ligands. The intensity ratio of $^5D_0\rightarrow{}^7F_2/^5D_0\rightarrow{}^7F_1$ for **E** (solid), **E**/C_{16}D (solid), and **E**/C_{16}D (film) is 2.04, 4.12, and 3.65, respective-

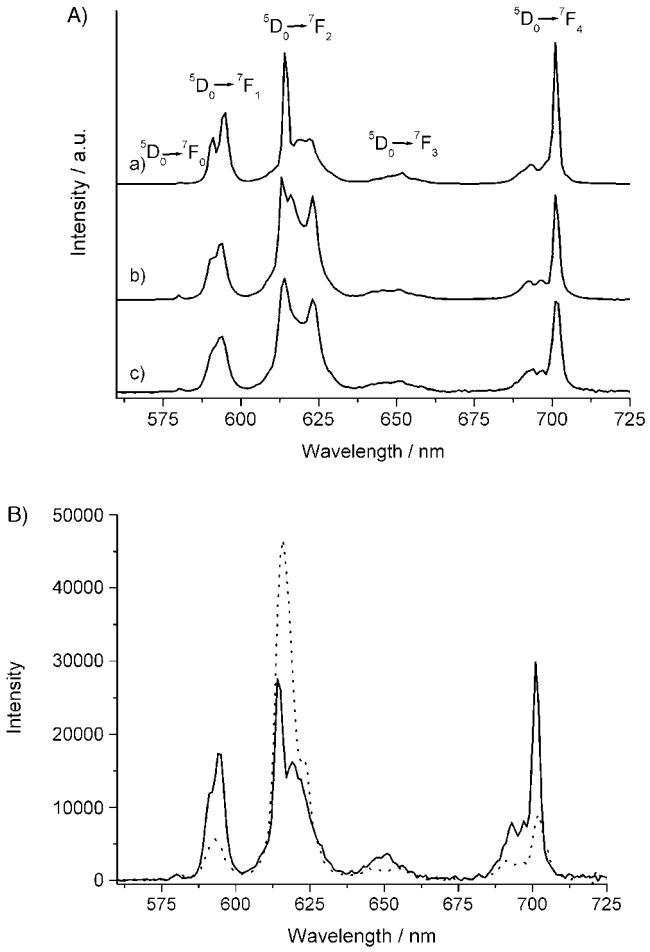

Figure 5. A) The emission spectra of a) **E** solid; b) **E**/C_{16}D solid, and c) **E**/C_{16}D film on quartz. B) The emission spectra of **E** (full line) and **E**/C_{16}D solution (dotted line) with the concentration of 0.2 mmol L^{-1} at room temperature.

ly. The fact suggests a more asymmetric environment occupied by the Eu^{3+} ion in the **E**/C_{16}D (solid) and **E**/C_{16}D (film) than in **E** (solid). The cationic heads of C_{16}D and K are different in terms of size and electronegativity. It is therefore expected that the interaction between C_{16}D and **E** will be different from that between K and **E**, which may result in the variation of the coordination of Eu^{3+} and the change of the symmetry of the site occupied by Eu^{3+}.[50] A further reason for the distortion of the site symmetry of Eu^{3+} may be related to the specific orientation of the polyanions in the structured films, which would also fit with the observed shift in the excitation spectrum. Our results also show that the interactions of the various surfactants with the polyanions influence the coordination environments and site symmetry of Eu^{3+} in different ways (Table 3). The transition probability between energy levels changes (to some degree) when the symmetry of the molecule is varied. As for the spectrum of **E** (solution) shown in Figure 5B, one could also find different emissions from those of **E** (solid). The intensity ratio of $^5D_0 \rightarrow {}^7F_2/{}^5D_0 \rightarrow {}^7F_1$ is increased to 2.32, where the water molecules lower the site symmetry of Eu^{3+}. There are large changes in the relative intensities of the emission bands in passing from **E**/C_{16}D solid to **E**/C_{16}D in diluted solutions. Taking the magnetic dipole $^5D_0 \rightarrow {}^7F_1$ transition as an internal standard, the most prominent variations are the strong increase in intensity of the $^5D_0 \rightarrow {}^7F_2$ and the symmetry-forbidden $^5D_0 \rightarrow {}^7F_0$ transition. The intensity ratio of $^5D_0 \rightarrow {}^7F_2/{}^5D_0 \rightarrow {}^7F_1$ is increased to 11.27, which is probably due to the disappearance of the orientation and ordered structure of the **E**/C_{16}D complex in the dilute chloroform solution and reorganization of the surfactants.

POMs, being good electron reservoirs, can accept electrons and be reduced to form colored mixed-valence-state materials. Ferrocene and viologen surfactants, when compared to normal surfactants, not only have big head groups which could provide special structural control of the POM/surfactant complexes, but also are good electron donors. We therefore expected the complexes consisting of POMs and functional organic surfactants to not only show photoluminescence, but also to exhibit (reversible) photochromism, that is, where photoinduced electron-transfer processes are not followed by major structural changes or further chemical evolution. However, we failed to detect any evidence of solid-state electron-transfer-induced photochromism. In addition, the luminescence of **E**/C_{15}F, **E**/C_{11}F, and **E**/C_{18}D complexes in the solid, solution, and film states is very weak. It is known[51] that functional organic groups close to surfaces may quench luminescence (see below).

The fluorescence emission decay curves of the complexes in the solid, film, and solution were obtained. All the $^5D_0$ decay curves are well-fitted by a single-exponential function, which proves the existence of only one Eu^{3+} local site symmetry. The experimental fluorescence lifetimes (τ) obtained from the exponential decay function are summarized in Table 3. The lifetimes of the complexes (both solids and films) are shorter than those of pure **E**. There are several possible origins for the observed lifetime shortening: a) water molecules coordinated to the Eu^{3+} first shell;[52] b) different environments of Eu^{3+};[50,53] and c) the dimension of the materials.[54] The number of water molecules coordinated to Eu^{3+} can be calculated with an estimated uncertainty of 0.5, according to the following empirical equation:[55] $q = 1.05(k_{tot} - k_r)$, where k_{tot} and k_r are the total transition and radiative rates, respectively. The values of k_{tot} and k_r can be obtained from the formulas depicted below. In our system, the q values for complexes consisting of simple surfactants are very low (< 0.4), which means that there are no water molecules in the first coordination sphere of Eu^{3+}. The main reason for lifetime shortening should therefore be the presence of organic cations (surfactants) that change the coordination environment of Eu^{3+} and lower the Eu^{3+} site symmetry. Compared to the respective complex solids, the complex films have the same compositions and very similar structures. The shorter lifetimes may therefore be a result, once again, of the macroscopic orientation of the materials influencing or inducing properties, such as the lateral electron transfer, thermal diffusion, and the formation of natural optical microcavities. For **E**/C_{18}D, **E**/C_{15}F, and **E**/C_{11}F com-

plexes, the functional organic groups' strong nonradiative deactivation of the excited state is the main factor for lifetime shortening.

By determining the absolute quantum yield (η) arising from the $^5D_0$ level and the respective radiative (k_r) and nonradiative (k_{nr}) rates, the previous conclusions can be quantified. The τ, k_r and k_{nr} rates are related through Equation (1), where k_r can be calculated by using Equation (2), [56,57] where $A_{0\rightarrow1}$ is Einstein's coefficient of spontaneous emission for the $^5D_0\rightarrow{}^7F_1$ transition, which is commonly referenced to 50 s^{-1} for solid samples,[58] and $14.65n^3$ s^{-1} (n is the refractive index of the solvent) for solutions,[59] and $\hbar\omega_{0\rightarrow J}$ and $S_{0\rightarrow J}$ are the energy and the integrated intensity of the $^5D_0\rightarrow{}^7F_J$ transition, respectively.

$$k_{tot} = \frac{1}{\tau} = k_r + k_{nr} \quad (1)$$

$$k_r = A_{0\rightarrow1}\frac{\hbar\omega_{0\rightarrow1}}{S_{0\rightarrow1}}\sum_{J=0}^{4}\frac{S_{0\rightarrow1}}{\hbar\omega_{0\rightarrow1}} \quad (2)$$

The absolute emission quantum yield η is given by Equation (3).

$$\eta = \frac{k_r}{k_r + k_{nr}} \quad (3)$$

The determined k_r, k_{nr}, and η values for complexes are listed in Table 3. In general, an increase in the k_r rate for all complexes in various states should be related with the presence of organic cationic surfactants. The complexes (in the solid and film state) consisting of simple surfactants have higher η values than **E** (solid). This results from the strong increase in the k_r rate and smaller variation in k_{nr}. Those complexes constructed with functional surfactants have much lower η values than **E** (solid); although the k_r rate increased, the k_{nr} rate shows a much bigger increase. This shows that the functional groups provide a strong nonradiative channel to quench the fluorescence. Compared to the responding solids, all the films show higher k_{nr} rates and lower η values, indicating that a new nonradiative channel is present in the films. In the solution state, only the **E**/$_{16}$D and **E**/C_{12}D complexes have higher η values than **E** (solution). This shows that not only the head groups and tails of the surfactants, but also the type of solvent has a great influence on the quantum yields η, and k_{nr} and k_{nr} rates. These results show that the photophysical properties of **E** can be changed easily by replacing the counterions with organic cationic surfactants. The amphiphilic cationic surfactants therefore not only play a structural role but also have a strong influence on photophysical properties of **E**.

Conclusion

In conclusion, we have shown that it is possible to generate highly ordered nanostructured materials from polyoxometaloeuropate and cationic surfactants by ionic self-assembly into a variety of phases.

Contrary to the parental POM species, these nanohybrid materials dissolve in organic solvents and form transparent films and bulk specimen, that is, a route is provided to transfer the useful POM properties into materials applications. The phase behavior of these complexes can easily be tuned by variation of the head groups and the alkyl-tail volume fraction of the complexing surfactant species.

These complexes show both room-temperature thermotropic liquid-crystalline phase behavior as well as room-temperature lyotropic liquid-crystalline phase behavior. Among them, **E**/C_{16}D and **E**/C_{12}D complexes exhibit typical columnar phases. To the best of our knowledge, this is the first report on the lyotropic liquid-crystalline phase behavior of polyoxometalate systems.

The photophysical behavior of **E** can furthermore be easily modified by complexation with cationic surfactants, although the electronic properties of the complexes still originate from **E**. Compared with those of **E**, fluorescence lifetimes of all complexes in solid powder, film, and solution states decrease due to the presence of surfactants. However, the fluorescence quantum yield of the complexes from alkyl surfactants shows an increase, whereas the complexes consisting of functional surfactants form strong nonradiative channels leading to the deactivation of the excited state.

It is assumed that the presented synthesis strategy can be easily extended to incorporate any kind of charged inorganic and organic tectonic unit with desired optical, electrical, or magnetic properties into supramolecular assemblies for practical applications.

Experimental Section

Materials: $K_{13}[Eu(SiW_9Mo_2O_{39})_2]\cdot15H_2O$ (**E**) and the ferrocenyl surfactant pentadecyldimethyl ferrocenylmethylammonium bromide (C_{15}FAB) were synthesized and purified as described in references [60,61]. Undecyldimethylferrocenylmethylammonium bromide (C_{11}FAB) was synthesized by mixing 1-bromoundecane (Aldrich) and (dimethylaminomethyl)-ferrocene (Aldrich) in a 1:1 molar ratio and keeping the mixture under constant reflux at 60 °C for 4 h in a nitrogen atmosphere. The reaction product was recrystallized three times from a mixture of chloroform and diethyl ether (volume ratio 1:5.25) to give a yellow, crystalline product in 28.7% yield. ^{1}H NMR (400 MHz, $CDCl_3$, 295 K): δ = 4.5 (s, 2H; Fc-CH_2-N(CH$_3$)$_2$), 4.3 (app. s, 4H; H$_{ferrocene}$), 4.2 (s, 5H; H$_{ferrocene}$), 3.3 (t, 2H; N(CH$_3$)-CH_2), 3.2 (s, 6H; N(CH_3)$_2$), 1.7 (m, 2H; CH$_2$-CH_2), 1.2 (m, 16H; CH$_2$-CH_2-CH$_2$), 0.85 ppm (t, 3H; CH$_2$-CH_3). Other surfactants (single tail) dodecyltrimethylammonium bromide (C_{12}TAB), hexadecyltrimethylammonium bromide (C_{16}TAB), (double tail) didodecyldimethylammonium bromide (C_{12}DAB), dihexadecyldimethylammonium bromide (C_{16}DAB), dioctadecylviologen dibromide (C_{18}DVB) were all purchased from Aldrich/Fluka (purity higher than 99%). Deionized water was used in the preparation of all complexes.

Synthesis and characterization: Since all the complexes of POM **E** with different surfactants are insoluble in water, they can be synthesized and purified by simple precipitation from water. Typical notation for the complexes is, for example, **E**/C_{12}T (**E**/surfactant, indicating tail length and with the counterion omitted in the case of the surfactant). A typical complexation procedure is given below.

E (0.2700 g, 0.04555 mmol) was dissolved in deionized water (15 mL, pH 5.2). Surfactant solution (40 mL, pH 5.2), for example, C_{12}TAB (0.1826 g, 0.5922 mmol), was added to the solution in 0.5 mL aliquots at 3 min intervals under vigorous stirring. The solution containing the precipitated complex was centrifuged and washed with deionized water (3× 30 mL) to remove the unbound counterions. The resulting purified complex was dried under vacuum at room temperature. The complex was dissolved in chloroform and filtered through a 0.45 μm PTFE filter film. The filtrate was then cast into a Teflon-coated holder and left to dry. After 24 h, the film was peeled off, powdered, and dried under vacuum. The results obtained by elemental analysis (C, N, and H) and thermogravimetric analysis (content of surfactant cation and crystallized water) indicate the following formulae: $(C_{34}H_{72}N)_{13}[Eu(SiW_9Mo_2O_{39})_2]\cdot 7H_2O$ (**E**/C_{16}D), $(C_{26}H_{56}N)_{13}[Eu(SiW_9Mo_2O_{39})_2]\cdot 7H_2O$ (**E**/C_{12}D), $(C_{19}H_{42}N)_{13}[Eu(SiW_9Mo_2O_{39})_2]\cdot 10H_2O$ (**E**/C_{16}T), $(C_{15}H_{34}N)_{13}[Eu(SiW_9Mo_2O_{39})_2]\cdot 10H_2O$ (**E**/C_{12}T), $(C_{28}H_{48}NFe)_{12}H[Eu(SiW_9Mo_2O_{39})_2]\cdot 4H_2O$ (**E**/C_{15}F), $(C_{24}H_{40}NFe)_{12}H[Eu(SiW_9Mo_2O_{39})_2]\cdot 4H_2O$ (**E**/C_{11}F) and $(C_{46}H_{82}N_2)_6H[Eu(SiW_9Mo_2O_{39})_2]\cdot 8H_2O$ (**E**/C_{18}D).

Chloroform solutions of the complexes (200 μL, 0.2 mmol L^{-1}) were directly cast onto quartz substrates for UV/Vis and fluorescence (FL) measurements. All films were prepared and dried under air for natural evaporation of chloroform (1 h) and then dried under vacuum at room temperature to remove the residual solvent. The mean thickness was estimated to be 500–550 nm by ellipsometry.

Elemental analyses (C, H, N, S) were performed on a Vario EL Elementar apparatus (Elementar Analysensysteme, Hanau, Germany).

IR spectra were recorded on a Nicolet Impact 400 Spectrometer. Powder and film samples were recorded in KBr discs and on BaF_2 slides (Maicom-Quarz GmbH), respectively.

UV/Vis spectra were recorded on a Perkin Elmer Lambda 2 dual-beam grating spectrophotometer with the slit width set at 2 nm.

Ellipsometric measurements were performed on silicon substrates by using a Multiskop (Optrel Germany, 2 mW He-Ne laser, $\lambda = 632.8$ nm; angle of incidence 70°).

Differential scanning calorimetry (DSC) was performed on a Netzsch DSC 204. The samples were examined at a scanning rate of 10 K min^{-1} by applying two heating and one cooling cycle. Thermogravimetric analyses (TGA) were performed on a Netzsch TG 209. The samples were examined at a scanning rate of 10 K min^{-1} between room temperature and 450 °C.

Phase behavior was studied by polarized light optical microscopy by using an Olympus BX 50 optical microscope equipped with an Olympus C-5060 wide zoom digital compact camera.

Small-angle X-ray scattering measurements were carried out with a Nonius rotating anode ($U = 40$ kV, $I = 100$ mA, $\lambda = 0.154$ nm) using image plates. With the image plates placed at a distance of 40 cm from the sample, a scattering vector range of $s = 0.07$–1.6 nm^{-1} was available. The 2D diffraction patterns were transformed into 1D radial averages. Wide-angle X-ray scattering (WAXS) measurements were performed by using a Nonius PDS120 powder diffractometer in transmission geometry. A FR590 generator was used as the source of $Cu_{K\alpha}$ radiation ($\lambda = 0.154$ nm). Monochromatization of the primary beam was achieved by means of a curved Ge crystal. Scattered radiation was measured by using a Nonius CPS120 position-sensitive detector. The resolution of this detector in 2θ is 0.018°.

Luminescent measurements were performed on a Spex-FL 212 spectrophotometer using a 450 W xenon lamp as the excitation source. The luminescent spectra of all solutions were recorded under identical conditions (such as concentrations and slit widths) so that the intensities of the excitation and emission bands are comparable. For the measurement of the fluorescence decay times, the sample was mounted in a 1 mm path-length quartz cell and excited by a pulse of a XeCl excimer laser at 308 nm. The beam has a pulse energy of approximately 10 mJ and a duration of 11 ns. The emitted light was passed through an interference filter (which removed the scattered light) and was detected at 90° to the exciting beam on a PIN Photodiode connected to an oscilloscope. The overall system response dominated by the photodiode in use was measured by the fluorescence of a white piece of paper (which has a very short lifetime of about 5 ns compared to the system response of 0.63 ms). The fluorescence decay curves of the samples were deconvoluted to the system response function by fitting a single exponential decay yielding decay times between 3.1 and 0.02 ms.

Acknowledgement

T.R.Z. thanks the Alexander von Humboldt Foundation for a postdoctoral fellowship. This work was supported by Max Planck Society and the Funds of the German Chemical Industry. Help with the X-ray measurements by Ingrid Zenke and technical help by Carmen Remde and Irina Shekova are gratefully acknowledged. We thank Professor Luís D. Carlos for discussions on the equation for radiative rate (k_r).

[1] M. T. Pope, A. Müller, *Angew. Chem.* **1991**, *103*, 56–60; *Angew. Chem. Int. Ed. Engl.* **1991**, *30*, 34–48.
[2] Special thematic issue on polyoxometalates: C. L. Hill (guest editor), *Chem. Rev.* **1998**, *98*, 1–387.
[3] *Polyoxometalate Chemistry: From Topology Via Self-Assembly to Applications* (Eds.: M. T. Pope, A. Müller), Kluwer Academic, Dordrecht, The Netherlands, **2001**.
[4] N. Casan-Pastor, P. Gomez-Romero, *Front. Biosci.* **2004**, *9*, 1759–1770.
[5] I. Ichinose, T. Asai, S. Yoshimura, N. Kimizuka, T. Kunitake, *Chem. Lett.* **1994**, *10*, 1837–1840.
[6] A. Stein, M. Fendorf, T. P. Jarvie, K. T. Muller, A. J. Benesi, T. E. Mallouk, *Chem. Mater.* **1995**, *7*, 304–313.
[7] G. G. Janauer, A. Dobley, J. Guo, P. Zavalij, M. S. Whittingham, *Chem. Mater.* **1996**, *8*, 2096–2101.
[8] A. Taguchi, T. Abe, M. Iwamoto, *Adv. Mater.* **1998**, *10*, 667–669.
[9] M. Clemente-Leon, B. Agricole, C. Mingotaud, C. J. Gomez-Garcia, E. Coronado, P. Delhaes, *Angew. Chem.* **1997**, *109*, 1143–1145; *Angew. Chem. Int. Ed.* **1997**, *36*, 1114–1116.
[10] E. Coronado, C. Mingotaud, *Adv. Mater.* **1999**, *11*, 869–872.
[11] S. Polarz, B. Smarsly, M. Antonietti, *ChemPhysChem* **2001**, *2*, 457–461.
[12] D. G. Kurth, P. Lehmann, D. Volkmer, H. Cölfen, A. Müller, A. Du Chesne, *Chem. Eur. J.* **2000**, *6*, 385–393.
[13] D. Volkmer, A. Du Chesne, D. G. Kurth, H. Schnablegger, P. Lehmann, M. J. Koop, A. Müller, *J. Am. Chem. Soc.* **2000**, *122*, 1995–1998.
[14] D. G. Kurth, P. Lehmann, D. Volkmer, A. Müller, D. Schwahn, *J. Chem. Soc. Dalton Trans.* **2000**, *21*, 3989–3998.
[15] W. F. Bu, H. L. Fan, L. X. Wu, X. L. Hou, C. W. Hu, G. Zhang, X. Zhang, *Langmuir* **2002**, *18*, 6398–6403.
[16] W. F. Bu, L. X. Wu, X. L. Hou, H. L. Fan, C. W. Hu, X. Zhang, *J. Colloid Interface Sci.* **2002**, *251*, 120–124.
[17] I. Moriguchi, K. Orishikida, Y. Tokuyama, H. Watabe, S. Kagawa, Y. Teraoka, *Chem. Mater.* **2001**, *13*, 2430–2435.
[18] T. R. Zhang, W. Feng, Y. Q. Fu, R. Lu, C. Y. Bao, X. T. Zhang, B. Zhao, C. Q. Sun, T. J. Li, Y. Y. Zhao, J. N. Yao, *J. Mater. Chem.* **2002**, *12*, 1453–1458.
[19] Y. D. Jin, L. H. Bi, Y. Shao, S. J. Dong, *Chem. Eur. J.* **2004**, *10*, 3225–3231.
[20] T. Yamase, *Chem. Rev.* **1998**, *98*, 307–325.
[21] V. Bekiari, P. Lianos, *Adv. Mater.* **1998**, *10*, 1455–1458.
[22] J. Kido, H. Hayase, K. Hongawa, K. Nagai, *Appl. Phys. Lett.* **1994**, *65*, 2124–2126.
[23] F. S. Richardson, *Chem. Rev.* **1982**, *82*, 541–552.
[24] O. Prat, E. Lopez, G. Mathis, *Anal. Biochem.* **1991**, *195*, 283–289.
[25] S. Lis, S. But, *Mater. Sci. Forum* **1999**, *315–317*, 431–438.
[26] C. F. J. Faul, M. Antonietti, *Chem. Eur. J.* **2002**, *8*, 2764–2768.
[27] C. F. J. Faul, M. Antonietti, *Adv. Mater.* **2003**, *15*, 673–683.

[28] F. Camerel, M. Antonietti, C. F. J. Faul, *Chem. Eur. J.* **2003**, *9*, 2160–2166.
[29] F. Camerel, P. Strauch, M. Antonietti, C. F. J. Faul, *Chem. Eur. J.* **2003**, *9*, 3764–3771.
[30] N. Nakashima, N. Yamada, T. Kunitake, J. Umemura, T. Takenaka, *J. Phys. Chem.* **1986**, *90*, 3374–3377.
[31] R. G. Nuzzo, F. A. Fusco, D. L. Allara, *J. Am. Chem. Soc.* **1987**, *109*, 2358–2368.
[32] C. Rocchoccioli-Deltcheff, M. Fournier, R. Franck, R. Thouvenot, *Inorg. Chem.* **1983**, *22*, 207–216.
[33] M. Clemente-Leon, B. Agricole, C. Mingotaud, C. J. Gomez-Garcia, E. Coronado, P. Delhaes, *Langmuir* **1997**, *13*, 2340–2347.
[34] R. Ballardini, E. Chiorboli, V. Balzani, *Inorg. Chim. Acta* **1984**, *95*, 323–327.
[35] R. D. Peacock, T. J. R. Weakley, *J. Chem. Soc. A* **1971**, *11*, 1836–1839.
[36] T. Nakanishi, M. Morita, H. Murakami, T. Sagara, N. Nakashima, *Chem. Eur. J.* **2002**, *8*, 641–1648.
[37] K. Okuyama, Y. Soboi, N. Lijima, K. Hirabayashi, T. Kunitake, T. Kaiyama, *Bull. Chem. Soc. Jpn.* **1988**, *61*, 1485–1490.
[38] A. S. Sonin, *J. Mater. Chem.* **1998**, *8*, 2557–2574.
[39] J. P. Gabriel, P. Davidson, *Adv. Mater.* **2000**, *12*, 9–20.
[40] J. C. P. Gabriel, F. Camerel, B. J. Lemaire, H. Desvaux, P. Davidson, P. Batail, *Nature* **2001**, *413*, 504–508.
[41] F. Livolant, A. M. Levelut, J. Doucet, J. P. Benoit, *Nature* **1989**, *339*, 724–726.
[42] F. Neve, O. Francescangeli, A. Crispini, J. Charmant, *Chem. Mater.* **2001**, *13*, 2032–2041.
[43] T. Yamase, M. Sugeta, *J. Chem. Soc. Dalton Trans.* **1993**, *5*, 759–765.
[44] G. Blasse, G. J. Dirksen, *J. Inorg. Nucl. Chem.* **1981**, *43*, 2847–2853.
[45] J. Wang, H. Wang, F. Y. Liu, L. S. Fu, H. J. Zhang, *J. Lumin.* **2003**, *101*, 63–70.
[46] P. C. R. Soares-santos, H. I. S. Nogueire, V. Félix, M. G. B. Drew, R. A. Sá Ferreira, L. D. Carlos, T. Trindade, *Chem. Mater.* **2003**, *15*, 100–108.
[47] O. L. Malta, H. J. Batista, L. D. Carlos, *Chem. Phys.* **2002**, *282*, 21–30.
[48] M. Dejneka, E. Snitzaer, R. E. Riman, *J. Non-Cryst. Solids* **1996**, *202*, 23–24.
[49] M. Nogami, Y. Abe, *J. Non-Cryst. Solids* **1996**, *197*, 73–78.
[50] J. Wang, H. H. Wang, L. S. Fu, F. Y. Liu, H. J. Zhang, *Thin Solid Films* **2002**, *415*, 242–247.
[51] J. W. Stouwdam, G. A. Hebbink, J. Huskens, F. C. J. M. van Veggel, *Chem. Mater.* **2003**, *15*, 4604–4616.
[52] W. F. Bu, L. X. Wu, X. Zhang, A. C. Tang, *J. Phys. Chem. B* **2003**, *107*, 13425–13431.
[53] F. L. Sousa, A. S. Ferreira, R. A. Sá-Ferreira, A. M. V. Cavaleiro, L. D. Carlos, H. I. S. Nogueia, T. Trindade, *J. Alloys Compd.* **2004**, *374*, 371–376.
[54] Y. L. Zhao, D. J. Zhou, G. Q. Yao, C. H. Huang, *Langmuir* **1997**, *13*, 4060.
[55] W. D. Horrocks, Jr., D. R. Sudnick, *Acc. Chem. Res.* **1981**, *14*, 384–392.
[56] L. D. Carlos, Y. Messaddeq, H. F. Brito, R. A. Sá-Ferreira, V. de Zea Bermudz, S. J. L. Ribeiro, *Adv. Mater.* **2000**, *12*, 594–598.
[57] R. A. Sá-Ferreira, L. D. Carlos, R. R. Goncalves, S. J. L. Ribeiro, V. de Zea Bermudz, *Chem. Mater.* **2001**, *13*, 2991–2998.
[58] M. F. Hazenkamp, G. Blasse, *Chem. Mater.* **1990**, *2*, 105–110.
[59] M. H. V. Werts, R. T. F. Jukes, J. W. Verhoeven, *Phys. Chem. Chem. Phys.* **2002**, *4*, 1542–1548.
[60] S. Lis, S. But, *J. Inclusion Phenom. Macrocyclic Chem.* **1999**, *35*, 225–231.
[61] S. S. Datwani, V. N. Truskett, G. A. Rosslee, N. L. Abbott, K. J. Stebe, *Langmuir* **2003**, *19*, 8292–8301.

Received: August 3, 2004
Published online: December 21, 2004

